



## Stability of fluids with shear-dependent viscosity in the lid-driven cavity

Simon Haque<sup>a</sup>, Iman Lashgari<sup>a</sup>, Flavio Giannetti<sup>b</sup>, Luca Brandt<sup>a,\*</sup>

<sup>a</sup>Linné FLOW Centre, KTH Mechanics, SE 100 44 Stockholm, Sweden

<sup>b</sup>DIMEC, University of Salerno, Via Ponte don Melillo, 84084 Fisciano (SA), Italy

### ARTICLE INFO

#### Article history:

Received 20 September 2011  
Received in revised form 15 February 2012  
Accepted 16 February 2012  
Available online 1 March 2012

#### Keywords:

Linear stability  
Non-Newtonian fluids  
Lid-driven cavity  
Sensitivity

### ABSTRACT

The classical problem of the lid-driven cavity extended infinitely in the spanwise direction is considered for non-Newtonian shear-thinning and shear-thickening fluids, where the viscosity is modeled by the Carreau model. Linear stability is used to determine the critical Reynolds number at which the two-dimensional base-flow becomes unstable to three-dimensional spanwise-periodic disturbances. We consider a square cavity, characterized by steady unstable modes, and a shallow cavity of aspect ratio 0.25, where oscillating modes are the first to become unstable for Newtonian fluids. In both cases, the critical Reynolds number first decreases with decreasing power-index  $n$  (from shear-thickening to shear-thinning fluids) and then increase again for highly pseudoplastic fluids. In the latter case, this is explained by the thinner boundary layers at the cavity walls and less intense vorticity inside the domain. Interestingly, oscillating modes are found at critical conditions for shear-thickening fluids in a square cavity while the shallow cavity supports a new instability of lower frequency for large enough shear-thinning. Analysis of kinetic energy budgets and structural sensitivity are employed to investigate the physical mechanisms behind the instability.

© 2012 Elsevier B.V. All rights reserved.

### 1. Introduction

The aim of this work is to numerically establish benchmark results for non-Newtonian shear-thinning and shear-thickening fluids in the classical lid-driven cavity flow, in the limit of infinitely wide cavities. A two-dimensional base flow solution is initially computed and its stability to three-dimensional disturbances investigated.

#### 1.1. The lid-driven cavity

The incompressible and Newtonian flow inside a lid-driven cavity is one of the most studied problems in fluid mechanics, even more since the establishment of computational fluid dynamics (CFDs). It describes the flow inside a rectangular box due to the tangential translation of one wall. Much attention has been directed to the cavity flow, both from an industrial and academic standpoint. Practical applications can be found in abundance in coating and mixing devices, as examples. The geometric simplicity of the problem makes it ideal for numerical discretization and computations, while the discontinuous mathematical boundary condition for the velocity leads to singular properties close to the corners of the moving lid and the two neighboring stationary walls. These features have made the lid-driven cavity a popular test case for

validation of Navier–Stokes solvers [1] and different numerical techniques. Most interestingly in this context, this flow has a rich behavior from the point of view of instabilities and bifurcations in closed systems.

Numerous previous studies have been conducted for this configuration both numerically and experimentally in Newtonian flows. Burggraf [2] aimed to investigate the Prandtl–Batchelor theorem for a square cavity. He used a relaxation method to compute solutions for Reynolds number ( $Re$ ) between 0 and 400. The results suggests that for higher  $Re$  an inviscid core vortex is formed, but secondary eddies develop near the bottom corners of the square for all  $Re$ .

Later, Pan and Acrivos [3] also used relaxation techniques to find creeping flow solutions close to the bottom corners of the cavity for aspect ratios  $\Gamma$  between 0.25 and 5, where  $\Gamma$  is defined as the ratio between the depth of the cavity and the length of the moving lid. Moreover, through experiments, they studied the flow for Reynolds number  $Re$  ranging from 20 to 4000 and concluded that for finite cavities and as  $Re \rightarrow \infty$  a single inviscid core will form and the corner eddies reduces significantly in size. For infinitely deep cavities the size of the primary vortex hinders the core from becoming fully inviscid even as  $Re \rightarrow \infty$  resulting in a balance between viscous and inertial forces in the cavity. The main assumption of this work [3] is two-dimensional flow.

Ghia et al. [4] and Schreiber and Keller [5] developed numerical methods to study the two-dimensional cavity with  $\Gamma = 1$  for  $Re$  up to 10,000. Both studies indicate that at such high velocities the

\* Corresponding author.

E-mail address: [luca@mech.kth.se](mailto:luca@mech.kth.se) (L. Brandt).

position of the core vortex moves toward the center of the square cavity and that the bottom left (BL) and right (BR) eddies grow in size. The BR is often referred to as the down stream secondary eddy (DSE).

Experiments of turbulent cavity flow were performed by Koseff et al. [6] for narrow cavity of spanwise aspect ratio  $\Lambda = 3$ , where  $\Lambda$  is defined as the ratio between the width and length of the moving lid. Kim and Moin investigated numerically the three-dimensional driven cavity with periodic boundary condition in the transversal (spanwise) direction, i.e. without end wall effects [7]. They added small random perturbations in the spanwise direction to the two-dimensional solutions and found that a pair of Taylor-Görtler-like (TGL) vortices appeared at  $Re$  around 900. This result was important because it demonstrated the flow becomes three-dimensional at high  $Re$  even without the presence of side walls in the spanwise direction.

Chiang et al. set out to map the eddy structure as function of the  $Re$  up to 1300 [8]. They considered a cavity with square cross section and  $\Lambda = 3$ . These authors show that the BL and DSE become developed at around  $Re = 50$ . At  $Re \approx 100$ , the corner eddies adjacent to the lid are formed. As the  $Re$  is increased it becomes evident that the two-dimensional nature of the flow undergoes a transition to a fully three-dimensional character in the form of a bifurcation from the steady state to an oscillating periodic state. Additional information can be found in a review paper by Shankar and Deshpande [9].

### 1.2. Stability of Newtonian cavity flow

Since it became generally accepted that the flow goes through a transition from two-dimensional to a three-dimensional state, few studies have been conducted to determine at which  $Re$  this transition occurs. As described by Albensoeder et al. [1], the flow undergoes symmetry breaking instabilities before becoming turbulent. The task is to find at what value of  $Re$  the first instability takes place when increasing  $Re$  from 0. This value of  $Re$  is often referred to as the critical Reynolds number  $Re_c$ .

Two innovative experiments were carried out by Aidun et al. [10,11]. In the first one, the transition from steady to unsteady state was studied when increasing  $Re$  from 100 to 2000. They concluded that the core vortex and DSE is stable up to a  $Re$  of around 825. They also found supercritical bifurcations from steady state to a pair of spiral waves at  $Re = 966$  with a dimensionless frequency of 0.1112. In the second set of experiments the velocity was decelerated from high speeds ( $Re \sim 2000$ ) to low ( $Re < 500$ ) to show that the steady states are not unique.

Ramanan and Homsy performed a numerical linear stability analysis of a square cavity with periodic boundary condition in the spanwise direction [12]. Similar to Kim and Moin, they first solved for the two-dimensional base flow and then perturbed it with three-dimensional disturbances. The result indicated a Görtler type instability close to the separating streamline between the core vortex and the DSE. The flow became unstable at  $Re \sim 594$  to a stationary mode with a transversal wave number  $\kappa \sim 2.12$ . Adding compressibility effects to the problem, Ding and Kawahara calculate the critical  $Re$  in a square cavity of infinite span [13]. They detected an oscillatory mode with non-dimensional frequency  $\omega = 0.08$  at  $Re = 920$  for  $\kappa = 7.4$ .

During the last decade, Kuhlmann and coworkers have produced a significant amount of work on the instability of the lid-driven cavity. As example, utilizing a cavity, where two lids move in different direction, they were able to show non-uniqueness of the two-dimensional steady flow [14]. In a following study they employed numerical simulations to establish the critical  $Re$  for a cavity with different  $\Gamma$  for  $\Lambda \rightarrow \infty$  [1]. By means of linear stability analysis these authors showed that the base flow becomes

unstable to four different three-dimensional modes depending on the aspect ratio. In particular, the square cavity suffers a stationary instability at  $Re$  around 786 and a  $\kappa$  of 15.4, hence quite different from results obtained by earlier research. These values were confirmed by experiments in a cavity with dimensions  $\Gamma = 1$  and  $\Lambda = 6.55$  and are now generally considered to be correct. Kuhlmann et al. asserted that this mode had been suppressed by end wall effects (due to short spanwise length) in previous investigations. The instability is found to be of centrifugal nature, localized on a streamline. The mechanism is inviscid and the viscosity play only a stabilizing role [15]. The localization is related to the spanwise wavenumber of the disturbance, the largest leading to more localized instability core.

### 1.3. Non-Newtonian cavity flow

To the best of our knowledge, only very few studies considered the simulation and stability analysis of non-Newtonian fluids in the lid-driven cavity, despite the importance in many applications. Most of the previous studies, moreover, consider polymeric flows. Pakdel et al. [16,17] experimentally analyzed the dynamic structure of the unstable cavity flow for spanwise aspect ratios between 0.25 and 4. These authors used an elastic fluid and Deborah number ( $De$ ) ranging from 0 to 35 to conduct their investigation. At low  $De$  the flow was two-dimensional and the core vortex moved upstream as  $Re$  was increased. For a high  $De$  the flow became unstable and three-dimensional. Grillet et al. [18] simulated the viscoelastic lid driven cavity flow to understand how elasticity varies the flow kinematics. Polymer stretches significantly downstream of the corners, resulting in a decrease in the rotational speed of the primary vortex. These authors also introduced a scaling law for the relation between the aspect ratio and the elastic instability. Cavity flow also has been used to validate numerical methods for non-Newtonian fluids. In this context, Pan and Hao [19] presented a method for stabilizing a finite element code used for high Weissenberg number flows. The Stokes flow of Oldroyd-B fluid in the lid-driven cavity is considered as a test case. Other examples of non-Newtonian fluids inside the cavity can be found in Yapaci et al. [20] and Santos et al. [21].

The only work on cavity flow of inelastic power-law fluids, we are aware of, is Mercan and Atalik [22]. These authors investigated the lid driven arc-shaped cavity flow of power-law fluids. They found formation of secondary vortices, for  $Re > 740$  when arc angle ratio  $r = 1/2$  and for  $Re > 800$  in the case of  $r = 1/3$ . The vortices grow or decay with the shear-thinning and the shear-thickening effects respectively.

### 1.4. Structural sensitivity

In the present work, the structural sensitivity analysis is employed to examine the instability mechanism of the lid-driven cavity flow to three dimensional modes. Giannetti and Lucini [23] introduced the concept of structural sensitivity and employed it to investigate the instability mechanism of the flow past a stationary cylinder. The core of instability, associated to the location in space, where a feedback provides the largest shift of the eigenvalues, is obtained as a superposition of direct and adjoint modes of the linearized stability operator. For the cylinder flow, the wave-maker of the instability is located in two lobes placed symmetrically downstream of the cylinder. Marquet et al. [24] also considered the maximum variation of the eigenvalues to analyze the sensitivity to base flow modifications of the flow past a circular cylinder. These authors determined the region that contributes to the onset of vortex shedding. To stabilize the flow Marquet et al. [25] and Pralits et al. [26] considered the sensitivity to steady forcing modifying the base flow: the sensitivity map is shown to

provide useful information to design successful passive control of the instability. In [26], the authors also examined the perturbation kinetic energy budget and compared it with the results of the sensitivity analysis. The two approaches are shown to give different results for the instability of the flow past a rotating cylinder: the region of maximum production of perturbation kinetic energy does not necessarily coincide with the core of the instability. Sensitivity analysis has been recently extended to globally stable flows, the so called noise amplifiers, in Brandt et al. [27]. Sipp et al. present a recent review about linear methods for sensitivity and control studies [28].

The paper is organized as follows. The flow geometry and governing equations are presented in Section 2, where the formulation for structural sensitivity of a non-Newtonian fluid is derived. The numerical method and validation are discussed in Section 3 before reporting the linear stability for the square cavity and the shallow cavity of aspect ratio 0.25. The paper ends with a summary of the main conclusions.

## 2. Problem formulation

### 2.1. The geometry

The geometry and generic flow behavior of the lid-driven cavity is depicted in Fig. 1. The lid has a width  $L_x$  and is moving with a constant velocity  $V$  in the  $x$ -direction, hence the Reynolds number  $Re$  is defined as:

$$Re = \frac{\rho L_x V}{\hat{\mu}_0},$$

where  $\rho$  and  $\hat{\mu}_0$  are the density and zero shear rate viscosity of the fluid. Furthermore, the aspect ratio is given by  $\Gamma = L_y/L_x$ . If a third  $z$ -direction is added then the spanwise aspect ratio is  $A = L_z/L_x$ , where  $L_z$  is the spanwise width of the cavity.

### 2.2. The viscosity model

As mentioned, an important aspect of this work which differentiates it from many earlier investigations is that it concerns non-Newtonian inelastic fluids. To examine non-Newtonian effects, a simple model, where viscosity is dependent on shear rate only is adopted and fluid elasticity is neglected. Hence, the constitute equation can be written as

$$\mu = \mu(\dot{\gamma}), \quad (1)$$

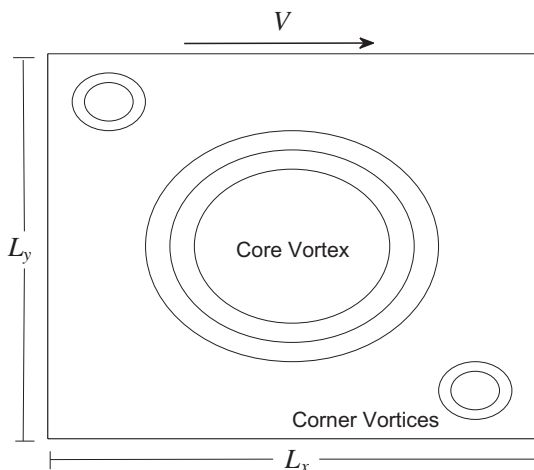


Fig. 1. Geometry and notation of the lid-driven cavity.

where  $\dot{\gamma}$  represents the second invariant of the strain-rate tensor, defined as  $\dot{\gamma} = (\frac{1}{2} \dot{\gamma} : \dot{\gamma})^{\frac{1}{2}}$ , with  $\dot{\gamma} = \nabla \mathbf{U} + \nabla \mathbf{U}^T$ . Thus, many empirical relations can be used to fit experimental data. Some examples, including the Cross and Bingham model can be found in [29].

For this project the so called Carreau model is employed: the connection between viscosity and shear rate is given by

$$\mu(\dot{\gamma}) = \frac{\hat{\mu}_\infty}{\hat{\mu}_0} + \left(1 - \frac{\hat{\mu}_\infty}{\hat{\mu}_0}\right) [1 + (\dot{\gamma}\lambda)^2]^{\frac{n-1}{2}}. \quad (2)$$

Here,  $\hat{\mu}_\infty$  and  $\hat{\mu}_0$  are the infinite shear rate and zero shear rate viscosity, respectively and the ratio of  $\hat{\mu}_\infty/\hat{\mu}_0$  is set to 0.001.

The results will be therefore presented in terms of the power index  $n$  and the time constant  $\lambda$ .  $\lambda$  is a dimensionless variable scaled by the cavity width and lid velocity. For a more detailed description of the parameters featured in Eq. (2) see [30].

### 2.3. Governing equations

The incompressible non-Newtonian lid-driven cavity flow is considered. The flow is induced by the tangential velocity of the top wall in the positive  $x$ -direction. The cavity length in the transverse  $z$ -direction is assumed to be infinite. Thus, the flow is governed by the Navier–Stokes and continuity equation which is expressed in non-dimensional form as

$$\frac{\partial \mathbf{u}}{\partial t} + \mathbf{u} \cdot \nabla \mathbf{u} = -\nabla p + \frac{1}{Re} \cdot \nabla [\mu(\nabla \mathbf{u} + \nabla \mathbf{u}^T)], \quad (3a)$$

$$\nabla \cdot \mathbf{u} = 0. \quad (3b)$$

The no-slip boundary conditions imposed on the problem are the following

$$\begin{cases} \mathbf{u} = 1 \mathbf{e}_x & \text{at } y = \frac{L_y}{L_x} = \Gamma & (a), \\ \mathbf{0} & \text{at } x = 0, x = 1 \text{ and } y = 0 & (b). \end{cases} \quad (4)$$

Note that for Eq. (4), the origin of the coordinate system has been placed in the bottom left corner of Fig. 1, and the boundary conditions are written in non-dimensional form.

### 2.4. Linear stability analysis

Since the cavity length is assumed infinite in the  $z$ -direction, Eq. (3) has a steady two-dimensional solution  $[\mathbf{U}_b, p_b] = [\mathbf{U}_b(x, y), p_b(x, y)]$ . A perturbation  $[\tilde{\mathbf{U}}, \tilde{p}] = [\tilde{\mathbf{U}}(x, y, z, t), \tilde{p}(x, y, z, t)]$  is added to this time independent state in order to perform the linear stability analysis. Thus, it is possible to decompose the flow variables into

$$\mathbf{u} = \mathbf{U}_b + \tilde{\mathbf{U}}, \quad (5a)$$

$$p = p_b + \tilde{p}. \quad (5b)$$

Furthermore, a similar formation is introduced for the viscosity

$$\mu = \mu_b + \tilde{\mu}, \quad (6)$$

where  $\mu_b = \mu_b(x, y)$  and  $\tilde{\mu} = \tilde{\mu}(x, y, z, t)$  are the base flow (steady state) and perturbation viscosity respectively. The perturbation viscosity is written as the first term of the Taylor series expansion of Eq. (2)

$$\tilde{\mu} = \dot{\gamma}_{ij}(\tilde{\mathbf{U}}) \frac{\partial \mu}{\partial \dot{\gamma}_{ij}}(\mathbf{U}_b). \quad (7)$$

Now, substituting Eqs. (5) and (6) into (3), subtracting the base flow variables and linearizing around  $[\mathbf{U}_b, p_b]$  yields a linear stability problem for the perturbations which can be formulated compactly as

$$\frac{\partial \tilde{\mathbf{U}}}{\partial t} + \mathbf{L}(\mathbf{U}_b, Re)\tilde{\mathbf{U}} + \nabla \tilde{p} = 0, \quad (8a)$$

$$\nabla \cdot \tilde{\mathbf{U}} = 0. \quad (8b)$$

In the above,  $\mathbf{L}(\mathbf{U}_b, Re)\tilde{\mathbf{U}}$  is defined by

$$\mathbf{L}(\mathbf{U}_b, Re)\tilde{\mathbf{U}} = \tilde{\mathbf{U}} \cdot \nabla \mathbf{U}_b + \mathbf{U}_b \cdot \nabla \tilde{\mathbf{U}} - \frac{1}{Re} \nabla \cdot [\mu_b(\nabla \tilde{\mathbf{U}} + (\nabla \tilde{\mathbf{U}})^T) + \tilde{\mu}(\nabla \mathbf{U}_b + (\nabla \mathbf{U}_b)^T)],$$

and homogenous boundary conditions are imposed to the disturbance velocities. As introduced, for example, by Albensoeder et al. [1] the general solution to Eq. (8) can be written as complex modes of the form:

$$\tilde{\mathbf{U}}(x, y, z, t) = \hat{\mathbf{U}}(x, y) \exp[\sigma t + i\kappa z] + c.c., \quad (9a)$$

$$\tilde{p}(x, y, z, t) = \hat{p}(x, y) \exp[\sigma t + i\kappa z] + c.c., \quad (9b)$$

where  $\kappa$  is the transverse wavenumber of the disturbance. A two-dimensional instability corresponds to  $\kappa = 0$ . Inserting the ansatz (9) into (8) finally produces a linearized general eigenvalue problem:

$$\sigma \hat{\mathbf{U}} + \mathbf{L}(\mathbf{U}_b, Re)\hat{\mathbf{U}} + \nabla \hat{p} = 0, \quad (10a)$$

$$\nabla \cdot \hat{\mathbf{U}} = 0. \quad (10b)$$

The complex eigenvalue  $\sigma$  contains information about the growth rate ( $RE\{\sigma\}$ ) and frequency ( $IM\{\sigma\}$ ) of the instability, whereas  $\hat{\mathbf{q}} = (\hat{\mathbf{U}}, \hat{p})$  is the eigenmode. Our goal is to determine for which  $Re$  and  $\kappa$  the growth rate first becomes positive for a given  $\Gamma$ ,  $n$  and  $\lambda$ . These values of  $Re$  and  $\kappa$  will be referred to as the critical Reynolds number ( $Re_c$ ) and wavenumber ( $\kappa_c$ ).

## 2.5. Structural sensitivity

Investigating the sensitivity of the unstable modes will give further insight about the origin of the instability. The theoretical framework is based on the work of Giannetti and Luchini [23] who introduce and define the wavemaker of the instability as the region in space, where a change in the structure of the problem causes the largest drift in the eigenvalues. Terms for the perturbation viscosity are added here. Introducing a small momentum force in the stability equations yields the following problem:

$$\sigma' \hat{\mathbf{U}}' + \mathbf{L}(\mathbf{U}_b, Re)\hat{\mathbf{U}}' + \nabla \hat{p}' = \delta H(\hat{\mathbf{U}}', \hat{p}'), \quad (11a)$$

$$\nabla \cdot \hat{\mathbf{U}}' = 0. \quad (11b)$$

As explained in [26],  $\delta H$  is a differential operator representing a force proportional to the local perturbation velocity:

$$\delta H(\hat{\mathbf{U}}', \hat{p}') = \delta M(x, y) \cdot \hat{\mathbf{U}}' = \delta(x - x_0, y - y_0) \delta M_0 \cdot \hat{\mathbf{U}}'$$

Here,  $\delta M_0$  is a coupling matrix and  $\delta(x - x_0, y - y_0)$  is the Kronecker delta function. The eigenvalue and eigenmode drifts are given as the expansion  $\sigma' = \sigma + \delta\sigma$ ,  $\hat{\mathbf{U}}' = \hat{\mathbf{U}} + \delta\hat{\mathbf{U}}$  and  $\hat{p}' = \hat{p} + \delta\hat{p}$ . Inserting these into Eq. (10) and neglecting higher order terms yields a linear equation for the eigenvalue drift:

$$\sigma \delta \hat{\mathbf{U}} + \mathbf{L}(\mathbf{U}_b, Re)\delta \hat{\mathbf{U}} + \nabla \delta \hat{p} = -\delta\sigma \hat{\mathbf{U}} + \delta M \cdot \hat{\mathbf{U}}, \quad (12a)$$

$$\nabla \cdot \delta \hat{\mathbf{U}} = 0. \quad (12b)$$

The Lagrange identity is introduced as a function of the differentiable direct field  $\mathbf{q} = (\mathbf{u}, p)$  and its corresponding adjoint field  $\mathbf{g}^+ = (\mathbf{f}^+, m^+)$ . More on adjoint methods can be found in [31,32]. By taking the inner product of Eq. (10) and the adjoint field and using differentiation by parts

$$[(\sigma \hat{\mathbf{U}} + \mathbf{L}(\mathbf{U}_b, Re)\hat{\mathbf{U}} + \nabla \hat{p}) \cdot \hat{\mathbf{f}}^+ + (\nabla \cdot \hat{\mathbf{U}}) \cdot \hat{m}^+] + [\hat{\mathbf{U}} \cdot (-\sigma \hat{\mathbf{f}}^+ + \mathbf{L}^+(\mathbf{U}_b, Re)\hat{\mathbf{f}}^+ + \nabla \hat{m}^+) + \hat{p} \nabla \hat{\mathbf{f}}^+] = \nabla \cdot \mathbf{J}(\hat{\mathbf{q}}, \hat{\mathbf{g}}^+), \quad (13)$$

where  $\mathbf{J}$  is the bilinear concomitant and  $\mathbf{L}^+$  is the adjoint linearized Navier–Stokes operator

$$\mathbf{J}(\hat{\mathbf{q}}, \hat{\mathbf{g}}^+) = \mathbf{U}_b(\hat{\mathbf{U}} \cdot \hat{\mathbf{f}}^+) + \frac{1}{Re} [\mu_b(\nabla \hat{\mathbf{f}}^+ + (\nabla \hat{\mathbf{f}}^+)^T) \cdot \hat{\mathbf{U}} - \mu_b(\nabla \hat{\mathbf{U}} + (\nabla \hat{\mathbf{U}})^T) \cdot \hat{\mathbf{f}}^+ - \tilde{\mu}(\nabla \mathbf{U}_b + (\nabla \mathbf{U}_b)^T) \cdot \hat{\mathbf{f}}^+] + \hat{m}^+ \hat{\mathbf{U}} + \hat{p} \hat{\mathbf{f}}^+,$$

and

$$\mathbf{L}^+(\mathbf{U}_b, Re)\hat{\mathbf{f}}^+ = \mathbf{U}_b \cdot \nabla \hat{\mathbf{f}}^+ - \nabla \mathbf{U}_b \cdot \hat{\mathbf{f}}^+ + \frac{1}{Re} [\mu_b(\Delta \hat{\mathbf{f}}^+ + (\Delta \hat{\mathbf{f}}^+)^T) + (\nabla \mathbf{U}_b + (\nabla \mathbf{U}_b)^T) \cdot \nabla \hat{\mathbf{f}}^+ \mathbf{B}(\mathbf{U}_b)].$$

where  $\mathbf{B}(\mathbf{U}_b)$  is an operator on the form:

$$\mathbf{B}(\mathbf{U}_b) = \begin{bmatrix} 2 \frac{\partial \mu}{\partial \gamma_{11}}(\mathbf{U}_b) \frac{\partial}{\partial x} + 2 \frac{\partial \mu}{\partial \gamma_{12}}(\mathbf{U}_b) \frac{\partial}{\partial y} \\ 2 \frac{\partial \mu}{\partial \gamma_{21}}(\mathbf{U}_b) \frac{\partial}{\partial x} + 2 \frac{\partial \mu}{\partial \gamma_{22}}(\mathbf{U}_b) \frac{\partial}{\partial y} \end{bmatrix}$$

The adjoint mode  $\hat{\mathbf{g}}^+(x, y) = (\hat{\mathbf{f}}^+, \hat{m}^+)$  satisfies the following system of equations

$$-\sigma \hat{\mathbf{f}}^+ + \mathbf{L}^+(\mathbf{U}_b, Re)\hat{\mathbf{f}}^+ + \nabla \hat{m}^+ = 0, \quad (14a)$$

$$\nabla \cdot \hat{\mathbf{f}}^+ = 0 \quad (14b)$$

Considering Eqs. (12) and (13) and integrating over the entire domain  $\mathcal{D}$  gives an estimate of the eigenvalue drift

$$-\delta\sigma \int_{\mathcal{D}} \hat{\mathbf{f}}^+ \cdot \hat{\mathbf{U}} dS + \int_{\mathcal{D}} \hat{\mathbf{f}}^+ \cdot \delta \mathbf{M} \cdot \hat{\mathbf{U}} dS = \oint_{\partial \mathcal{D}} \mathbf{J}(\hat{\mathbf{q}}, \hat{\mathbf{g}}^+) \cdot \mathbf{n} d\mathbf{l}. \quad (15)$$

The boundary conditions are chosen in such a way that the right hand side of Eq. (15) is zero. The sensitivity tensor  $\mathbf{S}$  is then introduced

$$\mathbf{S}(x_0, y_0) = \frac{\hat{\mathbf{f}}^+(x_0, y_0) \hat{\mathbf{U}}(x_0, y_0)}{\int_{\mathcal{D}} \hat{\mathbf{f}}^+ \cdot \hat{\mathbf{U}} dS}. \quad (16)$$

Note that  $\hat{\mathbf{f}}^+ \hat{\mathbf{U}}$  represents a dyadic product between the adjoint and direct mode. Combining Eq. (15) and (16) generates the final expression for the eigenvalue drift:

$$\delta\sigma(x_0, y_0) = \frac{\int_{\mathcal{D}} \hat{\mathbf{f}}^+ \cdot \delta \mathbf{M} \cdot \hat{\mathbf{U}} dS}{\int_{\mathcal{D}} \hat{\mathbf{f}}^+ \cdot \hat{\mathbf{U}} dS} = \frac{\hat{\mathbf{f}}^+ \cdot \delta \mathbf{M}_0 \cdot \hat{\mathbf{U}}}{\int_{\mathcal{D}} \hat{\mathbf{f}}^+ \cdot \hat{\mathbf{U}} dS} = \mathbf{S} : \delta \mathbf{M}_0 = S_{ij} \delta M_{0ij}. \quad (17)$$

The core of the instability can be found by studying different norms of the tensor  $\mathbf{S}$ . Here the spectral norm will be used.

## 2.6. Kinetic energy analysis

By performing an energy analysis, additional information about the instability mechanism can be extracted. Multiplying Eq. (8a) with the complex conjugate of the perturbation velocity  $\tilde{\mathbf{U}}^*$  (\* denotes the complex conjugate of the corresponding quantity) gives an equation for the evolution of the perturbation kinetic energy which in index notation can be written as

$$\begin{aligned} \tilde{U}_i^* \frac{\partial \tilde{U}_i}{\partial t} + \tilde{U}_i^* \tilde{U}_j \frac{\partial U_{bi}}{\partial x_j} + \tilde{U}_i^* U_{bj} \frac{\partial \tilde{U}_i}{\partial x_j} \\ = -\tilde{U}_i^* \frac{\partial \tilde{p}}{\partial x_i} + \frac{2}{Re} \tilde{U}_i^* \frac{\partial}{\partial x_j} (\mu_b e_{ij}) + \frac{2}{Re} \tilde{U}_i^* \frac{\partial}{\partial x_j} (\tilde{\mu} E_{ij}). \end{aligned} \quad (18)$$

Note here that  $U_{bi}$  and  $U_{bj}$  are the  $i$ th and  $j$ th component of the base flow velocity  $\mathbf{U}_b$ . Furthermore,  $e_{ij}$  and  $E_{ij}$  are the perturbation and base flow shear rate tensors

$$e_{ij} = \frac{1}{2} \left( \frac{\partial \tilde{U}_i}{\partial x_j} + \frac{\partial \tilde{U}_j}{\partial x_i} \right), \tag{19}$$

$$E_{ij} = \frac{1}{2} \left( \frac{\partial U_{bi}}{\partial x_j} + \frac{\partial U_{bj}}{\partial x_i} \right). \tag{20}$$

Finally, the kinetic energy budget reads

$$\begin{aligned} \frac{d(E_{kin})}{dt} = & \frac{\partial}{\partial x_j} \left[ -\frac{1}{2} U_{bj} \tilde{U}_i \tilde{U}_i^* - \frac{1}{2} (\tilde{U}_j^* \tilde{p} + \tilde{U}_j \tilde{p}^*) \right] + \frac{1}{Re} \mu_b (\tilde{U}_i^* e_{ij} + \tilde{U}_i e_{ij}^*) \\ & + \frac{1}{Re} E_{ij} (\tilde{U}_i^* \tilde{\mu} + \tilde{U}_i \tilde{\mu}^*) - \frac{1}{2} (\tilde{U}_i^* \tilde{U}_j + \tilde{U}_i \tilde{U}_j^*) \frac{\partial U_{bi}}{\partial x_j} - \frac{2}{Re} \mu_b (e_{ij} e_{ij}^*) \\ & - \frac{1}{Re} (\tilde{\mu} e_{ij}^* E_{ij} + \tilde{\mu}^* e_{ij} E_{ij}). \end{aligned} \tag{21}$$

Here  $E_{kin} = \frac{1}{2} (\tilde{U}_i \tilde{U}_i^*)$  is the kinetic energy. The first divergence term on the right hand side of Eq. (21) is the kinetic energy transport inside the domain. However since there is no net flux in a closed flow system like the cavity, it gives no global net contribution. The second and third terms are the production and dissipation of the perturbation kinetic energy, whereas the last expression is an additional term due the non-Newtonian properties of the flow. The latter is strictly positive for shear-thinning fluids and negative for shear-thickening. Note that the three dimensional effects only come into play in the energy dissipation since  $U_{b3} = W = 0$  and  $\frac{\partial}{\partial z} = 0$  for the base flow  $\mathbf{U}_b$ .

### 3. Numerical method

The numerical computations have been performed using a variant of the second order finite difference code developed by Giannetti and Luchini and described in [23]. To begin with the two-dimensional steady base flow is calculated by discretizing the flow variables on a staggered grid. Eqs. (3)–(4) are then solved using Newton–Raphson iteration, where the linear equations produced are inverted by means of a sparse LU decomposition. Next, the base flow solution is inserted into the perturbation Eq. (8) and the linear stability analysis is computed. Eigenvalues and modes of both the direct and adjoint field are computed by employing the Arnoldi shift and invert method. For all calculations a shift of  $2 + 0i$  has proved sufficient in order to find correct results (including oscillatory modes). Moreover, an eigenvalue tolerance of  $10^{-8}$  has been chosen to guarantee converged results. As mentioned above, the instability

occurs when the real part of the eigenvalue is larger than zero. A non-zero imaginary part corresponds to wave propagating in the z-direction, hence, the perturbation mode is non-stationary. Finally, the sensitivity, and thereby the core of the instability, is investigated by multiplying the direct and adjoint fields.

The eigenvalue strongly depends on  $Re$ ,  $\Gamma$ ,  $\kappa$ , the power-law index  $n$  and the time constant  $\lambda$ . The critical  $Re$  was found by applying the following strategy. Firstly, we select a relevant range for  $\Gamma$ ,  $n$  and  $\lambda$ . Secondly, an interval is chosen for the wavenumber  $\kappa$ , often between 0 and 20 (the wavenumber is assumed to be less than 20 since modes with higher  $\kappa$  are expected to be strongly damped [1]) and an incremental step size  $D_\kappa$ , usually selected to be 1 in a first approximation. Finally we apply a bisection procedure to find the critical Reynolds number while looping over different values of  $\kappa$ . Note however, that the wavenumber space is scanned only around the  $\kappa$  for which an instability is first encountered. The same procedure is then repeated with a lower tolerance to pinpoint the critical values of Reynolds and  $\kappa$ .

#### 3.1. Mesh

The square cavity of non-dimensional size  $L_x = L_y = 1$  will be mainly investigated in this work. Unless otherwise stated, a mesh size ( $n_x \times n_y$ ) of  $250 \times 250$  has been chosen for this case. Furthermore, a parabolic mapping is selected with the mesh being stretched by a ratio of 4 towards the boundaries of the geometry in both the x and y direction. Grid points are more densely clustered at the walls than in the center of the cavity as seen in 2a. This turned out to be necessary to obtain correct results in these high-gradient regions.

Analysis of a shallow cavity with aspect ratio  $\Gamma = 0.25$  has also been performed. The dimensions are therefore set to  $L_x = 1$ ,  $L_y = 0.25$ , where the number of grid points used is  $300 \times 75$ . Again parabolic stretching is used. Fig. 2b shows the grid used for these cases. Note that for the sake of clarity only every fourth point is shown in the figure.

#### 3.2. Code validation

The linear stability analysis has been validated by reproducing the results for Newtonian fluid in [1]. It can be seen from Table 1 that the present results based on the stretched  $250 \times 250$  grid are in good agreement, with an error below 1%.

Grid dependence for the non-Newtonian cases is checked by finding the critical  $Re$  and  $\kappa$  when  $\Gamma = 1$ ,  $n = 0.5$  and  $\lambda = 10$  for the several mesh sizes, see Table 2. The values reported in the Table confirm that the choice of grid points yields satisfactory results.

### 4. Results

In this section we examine the stability of the square and shallow cavity. Results are presented for values of the power-law index between  $0.4 \leq n \leq 1.4$  and time constant  $\lambda = 1, 10$  and  $100$ .

When  $n < 1$ , the fluid is shear thinning and the viscosity decreases with the shear rate. The opposite is true for shear-thickening fluids defined by values  $n > 1$ , while Newtonian fluids are

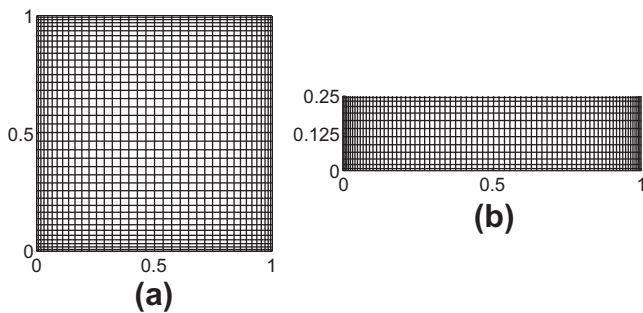


Fig. 2. Mesh used for square and shallow cavity. (a)  $\Gamma = 1$  and (b)  $\Gamma = 0.25$ .

Table 1

Comparison between the critical values presented by Albensoeder et al. [1] and the present results for a shallow cavity and a square cavity. (a) and (b) represent cases with  $150 \times 150$  and  $250 \times 250$  grid points respectively.

$\Gamma$	$Re_c$ [1]	$Re_c$	Error %	$\kappa_c$ [1]	$\kappa_c$	Error %	$\omega_c$ [1]	$\omega_c$	Error %
0.25	1152.7	1165	1.07	20.63	20.6	-0.15	2.27	2.25	-0.82
1(a)	786.3	789.1	0.36	15.43	15.2	-1.30	0	0	0
1(b)	786.3	786.74	0.06	15.43	15.4	-0.19	0	0	0

**Table 2**

Grid independence study. The tables reports the critical values at different resolution for shear-thinning fluids with  $n = 0.5$  and  $\lambda = 10$ .

Grid resolution	$Re_c$	Error %	$\kappa_c$	Error %
$150 \times 150$	330.7	6.23	13.9	-6.08
$200 \times 200$	317.5	1.99	14.5	-2.03
$250 \times 250$ (Reference)	311.3	-	14.8	-
$300 \times 300$	307.5	-1.22	14.8	0
$350 \times 350$	305	-2.02	14.8	0
$400 \times 400$	303.1	-2.63	14.8	0

retrieved when  $n = 1$  and the viscosity becomes independent of the shear rate.

#### 4.1. The square cavity, $\Gamma = 1$

The stream-wise velocity and streamlines of base-flow computed by Newton iterations has been initially compared with solutions obtained by direct numerical simulations (DNSs) with the code Nek5000 [33]; the data reported in Fig. 3 reveal good agreement. In the figure, we report as example the stream-wise velocity and streamlines for shear-thinning fluid with  $n = 0.4$ ,  $\lambda = 10$  and  $Re = 456$ .

Once the numerical calculations of the base flow is further validated, we proceed to the stability analysis. The neutral curve (critical  $Re$  vs.  $n$ ) is reported in Fig. 4a for the square cavity and different values of the parameter  $\lambda$ . Shear-thickening effects induce a significant increase of  $Re_c$ , this effect being more pronounced for larger values of  $\lambda$ . The opposite applies when  $n < 1$ ; in this case however the critical  $Re$  first decreases and then increases when increasing the shear-thinning properties (decreasing  $n$ ).

The viscosity varies locally inside the fluid and one can therefore define a local Reynolds number

$$Re_{loc} = \frac{\rho L_x V}{\hat{\mu}},$$

and the average Reynolds number

$$Re_{avg} = \frac{\int Re_{loc} dx dy}{A}, \quad (22)$$

where  $A$  is the total area of the cavity. Again,  $\mu(\dot{\gamma})$  is given by Eq. (2). The critical average Reynolds number is shown in Fig. 4b versus the index  $n$ . The large decrease of the critical  $Re$  when decreasing  $n$  is significantly reduced when considering  $Re_{avg}$  instead. As discussed below, this suggests that the same instability mechanism is at work for  $1.4 > n > 0.6$ . Conversely, the increase of critical Reynolds number at low  $n$  is now more evident. Interestingly, the trend is consistent for all values of  $\lambda$  considered and the difference almost disappear when re-scaling the neutral curves with the local viscosity.

The effect of the shear-dependent viscosity on the base flow is visualized by the streamwise component of  $\mathbf{U}_b$  and streamlines displayed in Fig. 5. The boundary layer at the lid becomes thinner and thinner when decreasing  $n$  while the magnitude of the negative counterflow at the lower wall decreases. This is also associated to weaker vorticity in the center of the cavity.

The circular frequency and the spanwise wavenumber pertaining to the first instability are reported in Fig. 6. Steady modes are the first to become unstable in the case of Newtonian fluid and this is still valid for shear-thinning fluids, see Fig. 6a. However, non-stationary modes are first unstable for  $n > 1.2$  for all  $\lambda$  investigated. These modes have a lower spanwise wavenumber as displayed in

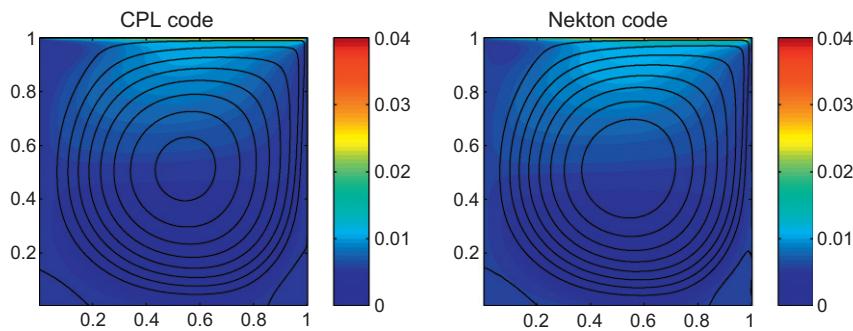


**Fig. 3.** Comparison of the nonlinear base flow computed with direct numerical simulations (Nekton code) and Newton iterations (CPL code) for  $n = 0.4$ ,  $\lambda = 10$  and  $Re = 456$ . The contours indicate streamlines.

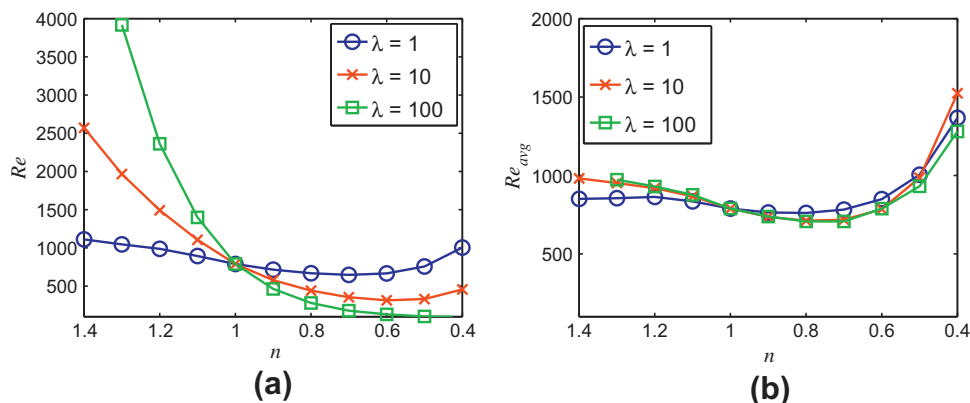


**Fig. 4.** (a) Critical Reynolds number versus the index  $n$  for different values of  $\lambda$ . (b) Average Reynolds number  $Re_{avg}$  at neutral conditions versus  $n$ .

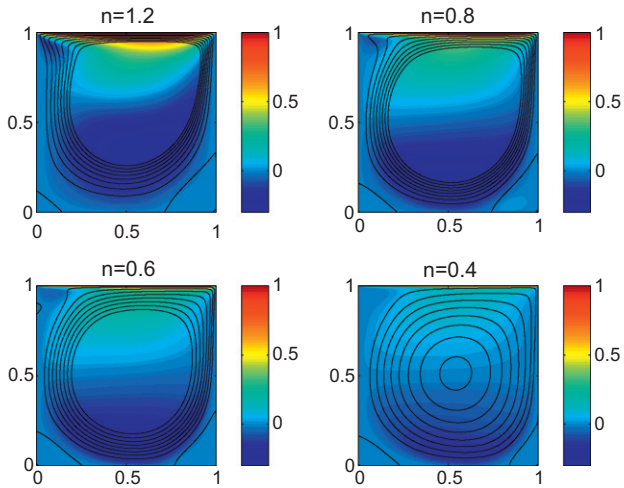


Fig. 5. Distribution of the x-component of the baseflow velocity  $U_b$  and streamlines at fixed  $Re = 600$  for  $\Gamma = 1$  and  $\lambda = 10$  for the indicated values of  $n$ .

Fig. 6b. Interestingly, a mode of even higher frequency and lower spanwise wave-number  $\kappa$  appears as the most dangerous when  $n = 1.4$ . The frequency and wave-number are more or less independent of  $\lambda$  and of the power index  $n$  when steady modes appear first. In the case of  $n = 1.15$ , the first unstable mode is stationary with high spanwise wave-number for  $\lambda = 1$  while it is oscillatory with a lower spanwise wave-number for  $\lambda = 10$  and  $\lambda = 100$ .

Direct and adjoint modes indicate, where in the flow field the perturbation amplitude is maximized and the location of highest receptivity. The magnitude of the unstable modes for  $n = 1.4$ ,  $n = 1$  (Newtonian) and  $n = 0.4$  are displayed in Fig. 7. For  $n = 1.4$ , which is associated to higher frequency and longer spanwise scale, the mode appears as a large vortex in the center of the cavity. This mode enhances and decreases the amplitude of the base flow vortex periodically in time and spanwise direction. For the Newtonian fluid, velocity perturbations are mainly found on the left side of the cavity; a finding common to modes in the range  $1.1 > n > 0.4$ , where the critical Reynolds number  $Re_{avg}$  is almost constant. When further decreasing the power-index  $n$  we see that the perturbation is now located on a thinner region on the lower wall and partially on the

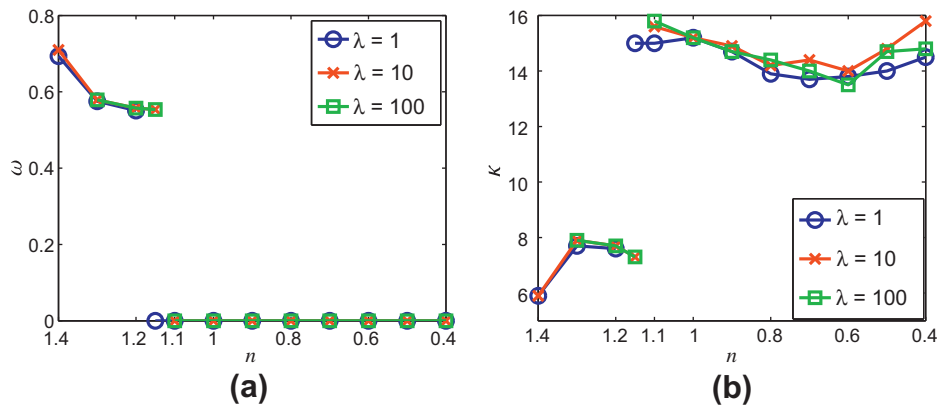


Fig. 6. (a) Frequency  $\omega$  and (b) critical spanwise wavenumber  $\kappa$  of the first instability mode for different values of  $\lambda$  plotted versus the power index  $n$ .

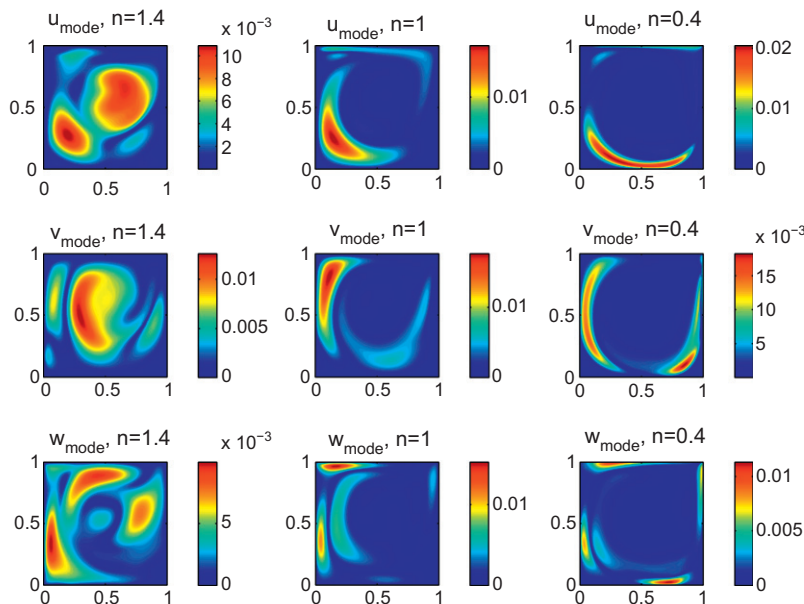


Fig. 7. Magnitude of the x-, y- and z-velocity components ( $u$ ,  $v$  and  $w$ ) of the first instability mode for (a)  $n = 1.4$ , (b)  $n = 1$  and (c)  $n = 0.4$ ,  $\lambda = 10$ .

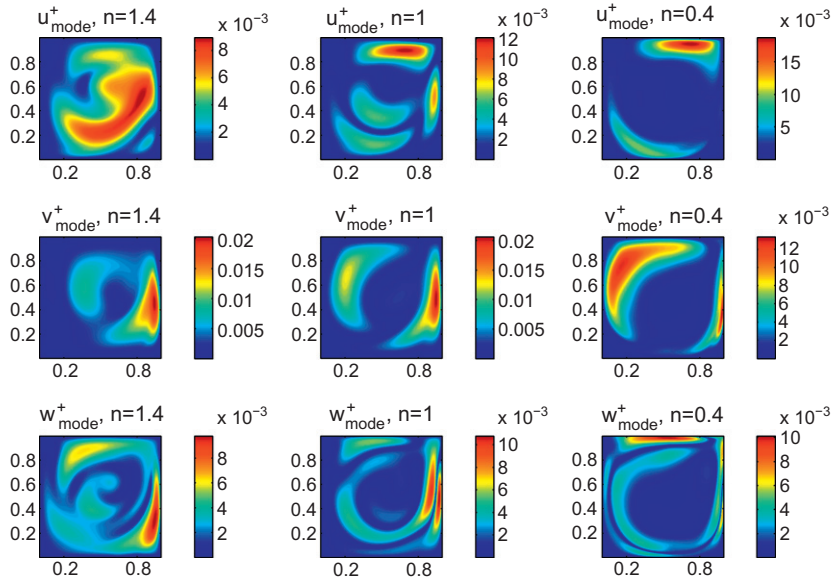


Fig. 8. Magnitude of the  $x$ -,  $y$ - and  $z$  components ( $u^+$ ,  $v^+$  and  $w^+$ ) of the adjoint of the first instability mode for (a)  $n = 1.4$ , (b)  $n = 1$  and (c)  $n = 0.4$ ,  $\lambda = 10$ .

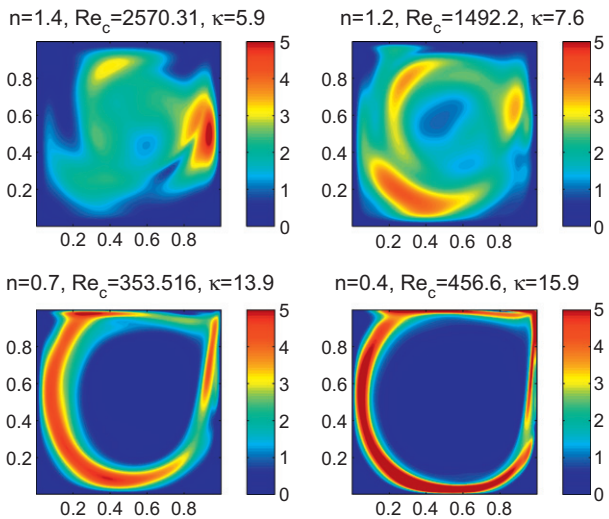


Fig. 9. Structural sensitivity for the first instability along the neutral curve for  $\lambda = 10$  and the indicated values of  $n$ .

right side. A second peak is formed in the bottom right corner of the cavity for the  $v$ -component of the velocity perturbation.

The adjoint modes concerning the first instability in shear-thickening, Newtonian and shear-thinning fluids are shown in Fig. 8. For the non-stationary modes,  $n = 1.4$ , the receptivity to forcing in the  $y$ -direction is strongest and located on the right side of the cavity. The receptivity to momentum forcing in  $x$ -direction is instead more diffuse, placed in the middle of the cavity. Forcing in the spanwise direction is more effective at the right wall. Considering the Newtonian fluid, we see that the region of highest receptivity is located on the corner opposite to that, where the disturbance is largest. The adjoint  $v^+$  and  $w^+$  is stronger on the right wall of the cavity. In the case of strong shear-thinning, the flow is most sensitive to forcing in the  $x$ -direction at the upper wall, while normal forcing is most efficient on the left side of the cavity.

Next, the structural sensitivity is presented. As introduced above, its distribution provides important information about the instability mechanism. Results for both shear-thinning and

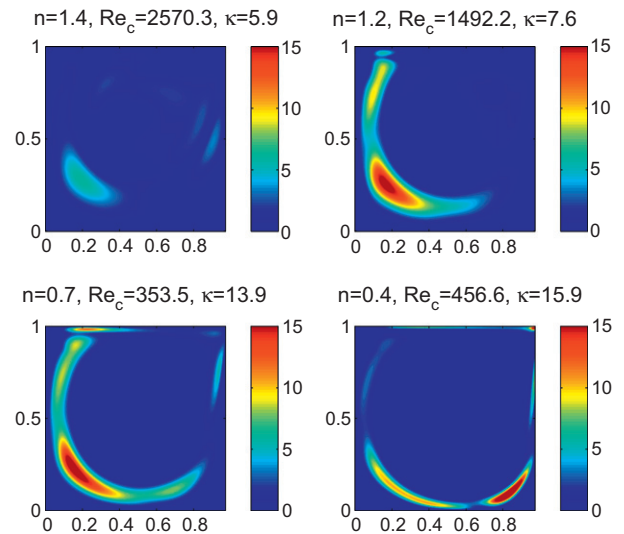


Fig. 10. Density of production of perturbation kinetic energy for selected values of  $n$  and  $\lambda = 10$  at neutral conditions.

shear-thickening fluids are presented in Fig. 9. As we increase shear-thinning, the region at the core of the instability is getting thinner but still consists of a ring, wrapping around a streamline inside the cavity. At large  $\kappa$ , the structural sensitivity identifies one specific streamlines, that supporting the inviscid centrifugal instability [15]. In the case of shear-thickening fluid and unsteady modes, we see that the wave-maker is located on the lower-left corner when  $n = 1.2$ , whereas it moves to the right wall for  $n = 1.4$ .

We now present the analysis of the perturbation kinetic energy budget. As introduced in Section 2.6 the kinetic energy budget, i.e. Eq. (21), is given by the sum of production, dissipation and additional production terms related to the varying viscosity. The density of energy production associated to the base flow shear is reported in Fig. 10, again for  $\lambda = 10$  at neutral conditions. We choose here to display four representative cases: two unsteady modes in shear-thickening fluids ( $n = 1.2$  and  $n = 1.4$ ), the case with  $n = 0.7$  indicative of Newtonian and weakly shear-thinning fluids

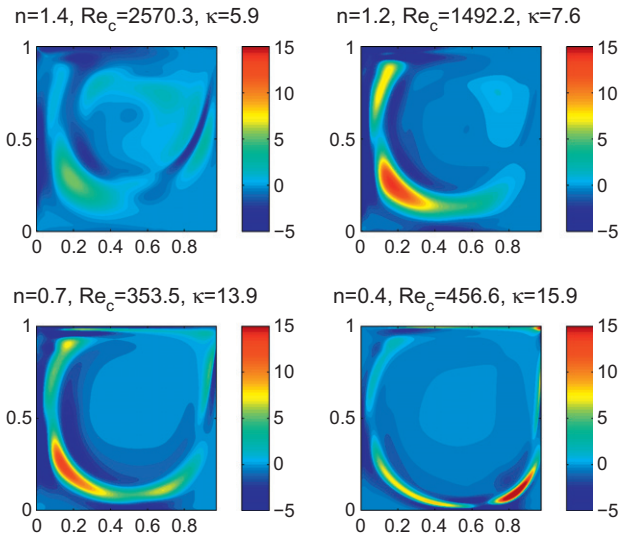


Fig. 11. Density of the total energy production for the indicated values of  $n$  and  $\lambda = 10$  at neutral conditions.

and  $n = 0.4$  representing the region of increasing critical Reynolds number. One can see from the figure that the Newtonian fluid actually has the largest energy production and that its spatial distribution is almost independent on the power index  $n$ . The spatial

distribution of the additional energy production due to non-Newtonian effects is most relevant on the left and lower side of the cavity for the lowest  $n$  considered (not shown here).

The sum of all production and dissipation terms is displayed in Fig. 11 for the same cases as before and at neutral conditions. Production is dominating in the lower left corner for intermediate values of  $n$ . In the case of strong shear-thinning, the peak of total production is on the lower right corner, whereas for unsteady modes ( $n = 1.4$ ) the peak of positive production is more diffuse towards the lower left corner. Negative production, dissipation, appears usually in this layers close to the regions of highest positive production and on the upper left corner. It is also interesting to note that in this close configuration the wave-maker of the instability and the region of largest production of perturbation kinetic energy almost overlap; this was not the case for the cylinder flow as shown in [26].

Finally, we integrate the densities of the different energy terms over the domain. The results are shown in Fig. 12 for  $\lambda = 10$  at neutral condition and for fixed  $Re = 600$  and  $\kappa = 15$ . In 12a we see that production associated to the base flow shear and dissipation have maximum around  $n = 1$  and decrease when adding shear-dependent viscosity. The decrease in dissipation magnitude can be associated to the vorticity of the instability mode, while the reduction in production to the localization of the perturbation when  $n < 1$  and to the weaker base shear when  $n > 1$ . The additional production term becomes relevant when  $n < 0.6$ . It is also instructive to study the energy budget at fixed Reynolds number. In this case, the sum of the different terms reveals whether the mode is stable

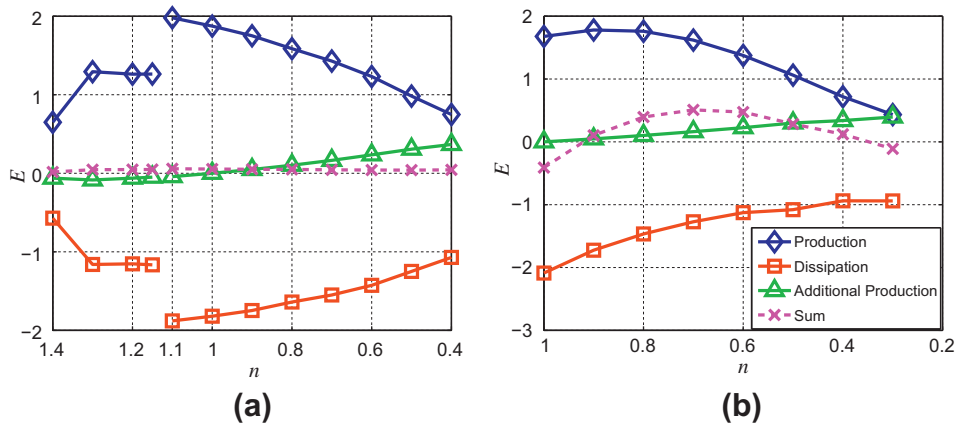


Fig. 12. Budget of production of perturbation kinetic energy for  $\lambda = 10$ . (a) Budget at neutral condition and (b) at fixed  $Re = 600$  and  $\kappa = 15$ .

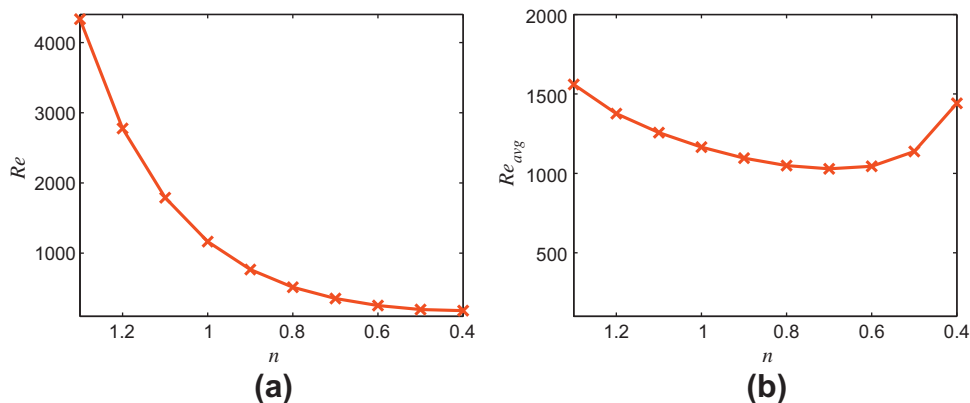


Fig. 13. (a) Critical Reynolds number versus the index  $n$  and (b) Average Reynolds number  $Re_{avg}$  at neutral conditions versus  $n$  for  $\Gamma = 0.25$  and  $\lambda = 10$ .

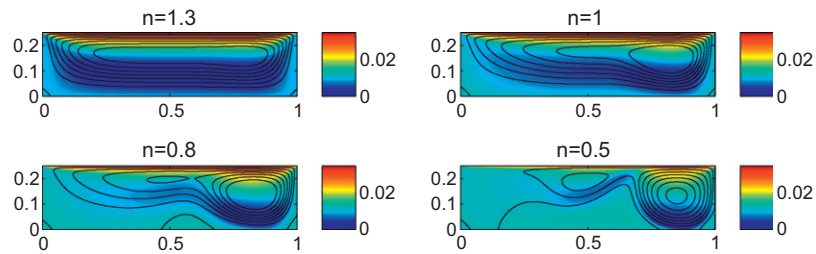


Fig. 14. Distribution of the x-component of the baseflow velocity  $U_b$ , and streamlines at fixed  $Re = 500$  for  $\Gamma = 0.25$ ,  $\lambda = 10$  and the values of  $n$  indicated.

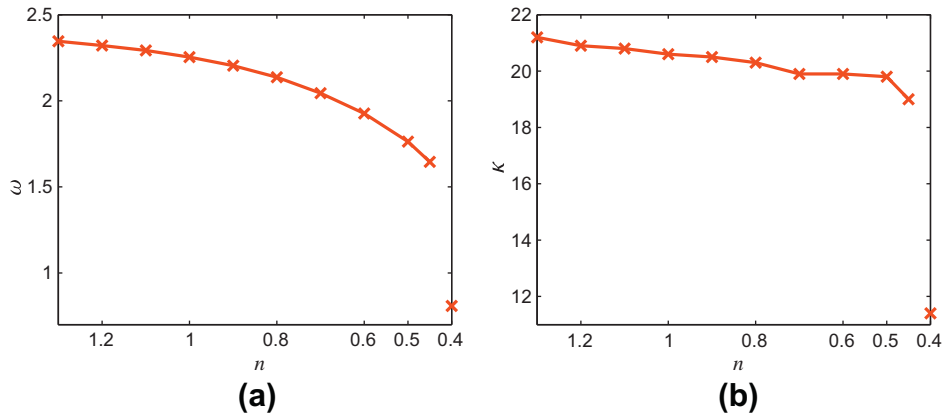


Fig. 15. (a) Frequency  $\omega$  and (b) critical spanwise wavenumber  $\kappa$  of the first instability mode plotted versus the power index  $n$  for  $\Gamma = 0.25$  and  $\lambda = 10$ .

or unstable since it can be related to the real part of the eigenvalue. For the case depicted in the figure, the flow is unstable for  $0.9 > n > 0.4$ . In addition to the expected increase of the additional production for lower values of  $n$ , we notice a decrease of the classic production with shear-thinning. This is due to the spatial de-correlation between the region of largest disturbance (lower and left wall, cf. Fig. 7) and the region of largest shear (upper wall, cf. Fig. 5).

Combining the results presented above, we can conclude that the instability mechanism is not significantly changed for weak shear-thinning and shear-thickening effects. Indeed, the  $Re_{avg}$  is almost constant in this range, steady modes are the most unstable and the instability wave-maker is similar. When further increasing the shear-thinning properties, we see a surprising increase of the critical Reynolds number based on the zero-shear-rate viscosity. This can be explained by the fact that the region of largest shear become more and more localized close to the wall and the

base-flow vorticity is weaker towards the center of the cavity and on the left side: in this case very large local Reynolds number (very low local viscosity) is necessary to overcome dissipation with the relevant contribution from the extra production terms associated to the shear-thinning effects. Interestingly, we notice that unsteady modes are the first to become unstable when the power index  $n$  is above 1.2 (or above 1.15 for large values of material time constant) with modes significantly longer in the spanwise direction. Finally, we note that the instability characteristics are found to vary with the power index  $n$ , while no significant qualitative variations are found with respect to the time constant  $\lambda$ .

#### 4.2. The shallow cavity, $\Gamma = 0.25$

We now consider the shallow cavity of aspect ratio  $\Gamma = 0.25$ , as in [1], where the first instability mode is time-periodic in Newtonian fluids. Computations have been performed with  $\lambda = 10$ ; as

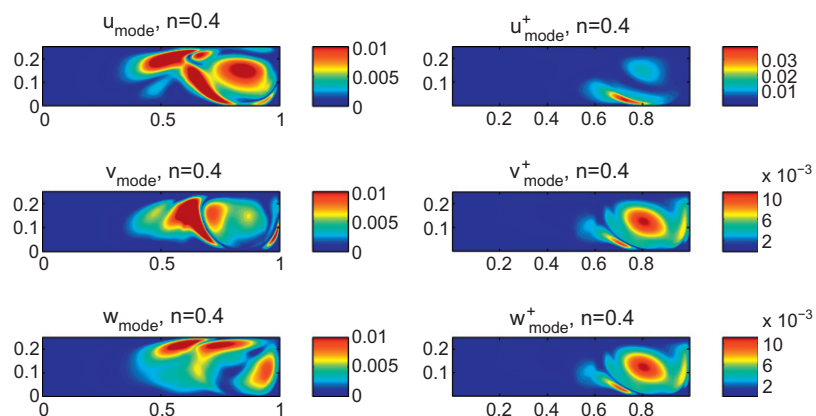


Fig. 16. Magnitude of the x-, y- and z-velocity components of the first instability of direct ( $u$ ,  $v$  and  $w$ ) and adjoint ( $u^+$ ,  $v^+$  and  $w^+$ ) modes for  $n = 0.4$ ,  $\Gamma = 0.25$  and  $\lambda = 10$ .

shown above this parameter does not seem to significantly affect the physics of the instability, the main variations coming from the power index  $n$ .

The neutral curves are first displayed in Fig. 13 both in terms of zero-shear rate viscosity, Reynolds number  $Re$ , and average viscosity, average Reynolds number  $Re_{avg}$ . The critical Reynolds number decreases from shear-thickening to shear-thinning fluids (decreasing  $n$ ), whereas critical values of the average Reynolds number first decrease and then increase with a minimum at  $n \approx 0.7$ , similarly to what observed for the square cavity.

The effect of shear-thinning viscosity on the two-dimensional base flow is depicted in Fig. 14, where we report the  $x$ -component of the baseflow velocity  $U_b$  and streamlines for four values of  $n$ . As

$n$  decreases we clearly see that the main vortex moves to the right side of the cavity. In addition, and in analogy to the case of the square cavity, the boundary layer at the moving lid becomes thinner at lower  $n$ . The lid drives flow towards the right wall and by viscous forces positive  $x$ -momentum is transferred towards the center of the cavity. For the continuity constraint, negative velocity is generated at the lower side of the cavity. When increasing shear-thinning, less momentum is transferred to the fluid and therefore the counter-flow only reaches half of the cavity.

Unlike the square cavity, all critical modes are oscillatory for the shallow cavity. The frequency and spanwise wavenumber of the neutral modes are reported in Fig. 15; here one can see that the value for  $\kappa_c$  and  $\omega_c$  drops continuously with decreasing power-law

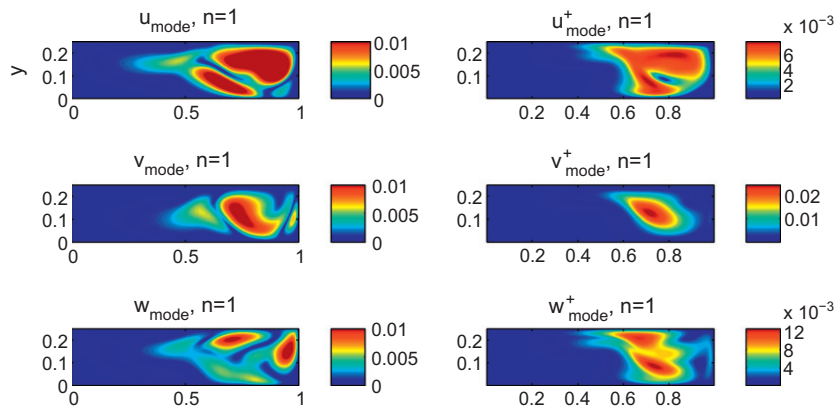


Fig. 17. Magnitude of the  $x$ -,  $y$ - and  $z$ -velocity components of the first instability of direct ( $u$ ,  $v$  and  $w$ ) and adjoint ( $u^+$ ,  $v^+$  and  $w^+$ ) modes for  $n = 1$ ,  $\Gamma = 0.25$  and  $\lambda = 10$ .

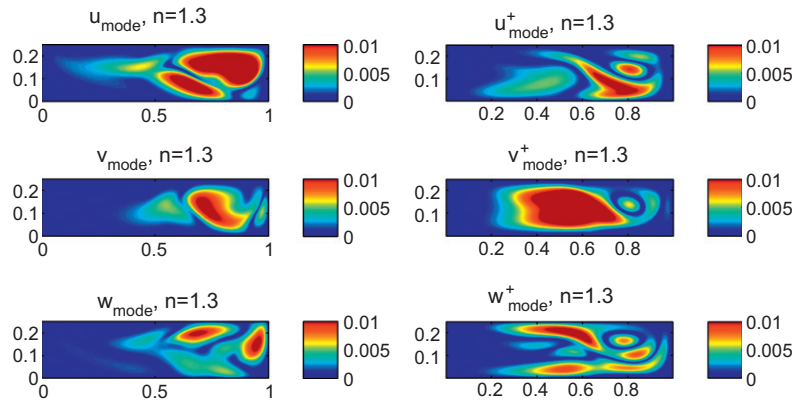


Fig. 18. Magnitude of the  $x$ -,  $y$ - and  $z$ -velocity components of the first instability of direct ( $u$ ,  $v$  and  $w$ ) and adjoint ( $u^+$ ,  $v^+$  and  $w^+$ ) modes for  $n = 1.3$ ,  $\Gamma = 0.25$  and  $\lambda = 10$ .

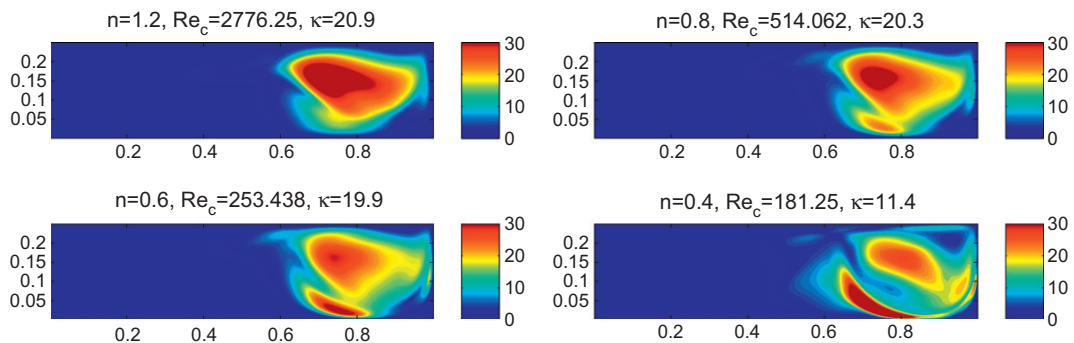


Fig. 19. Structural sensitivity for the first instability along the neutral curve for  $\Gamma = 0.25$  and  $\lambda = 10$ . The critical values are reported in the plots.

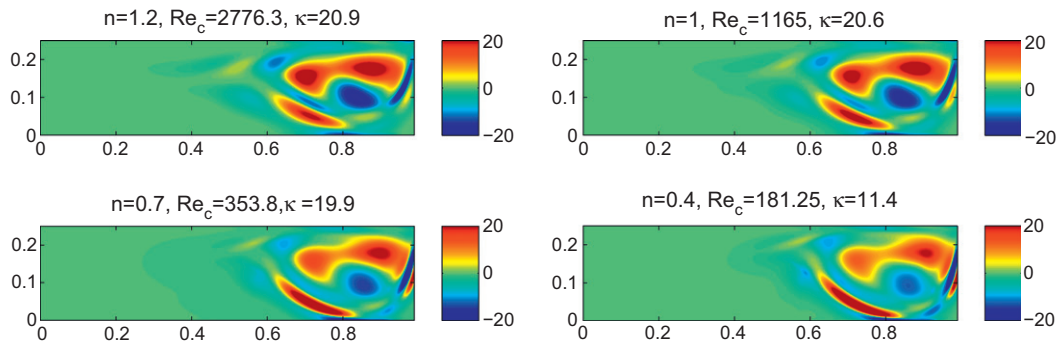


Fig. 20. Density of the total energy production for the indicated values of  $n$  and  $\lambda = 10$  at neutral conditions.

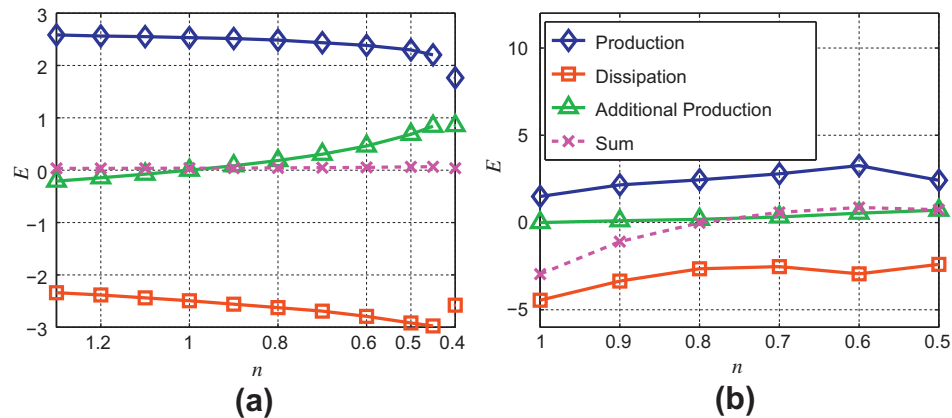


Fig. 21. Budget of production of perturbation kinetic energy for the shallow cavity  $\Gamma = 0.25$  and  $\lambda = 10$ . (a) Budget at neutral condition and (b) at fixed  $Re = 500$  and  $\kappa = 20$ .

index, from about  $\kappa = 21.2$  and  $\omega = 2.34$  respectively, until suddenly at  $n = 0.4$  the first instability appears to have a long-wavelength ( $\kappa \approx 11$ ) and low-frequency ( $\omega \approx 0.7$ ).

The shape of the direct and adjoint modes are shown in Fig. 16 for shear-thinning fluids. The region of largest fluctuations is seen to move from the top-right corner to the center of the cavity (left side of the big vortex displayed in Fig. 14) when shear-thinning increases and the instability mode has a significantly lower frequency. In all cases, velocity fluctuations are detectable on the right-half of the cavity. The corresponding adjoint modes reveal a certain overlap with the direct modes; Forcing in the  $x$ -direction at the lower wall is the most effective way to excite the slow oscillatory mode at  $n = 0.4$ .

The direct and adjoint modes pertaining a Newtonian fluid and shear-thickening fluid are displayed in Figs. 17 and 18. It is seen here that the shape of the direct modes is not affected by the non-Newtonian properties of the fluid, while it is interesting to note that for the case with  $n > 1$ , the adjoint modes are significant also in the left-half of the cavity. This can be explained by the fact that the base-flow vortex now extends throughout the cavity and it not only localized on the right side of it, as seen in Fig. 14.

The structural sensitivity, the core of the instability, is shown in Fig. 19 at neutral conditions and different values of  $n$ . The area of largest sensitivity is always located on the right-side of the cavity and decreases as the power-law index is reduced. Further, the maximum moves from the region close to the upper wall to that close to the lower wall for  $n > 0.6$ . This effect is found to be associated to the increase of the critical  $Re_{avg}$ , shown in Fig. 13b.

The spatial distribution of the sum of the different terms in the budget for the perturbation kinetic energy are presented in Fig. 20. It can be seen that the production mainly stems from the binocular- and banana-shape regions close to the upper and lower

wall respectively, whereas dissipation occurs in a thin stripe between the regions of largest positive production. As for the square cavity, we note that the wave-maker identified by the structural sensitivity and the areas more energetically active overlap. As discussed above, the core of the instability shifts from the upper to the lower wall as shear-thinning increases.

Finally, as for the square cavity, we examine the total budget of the perturbation kinetic energy, Fig. 21. As for the square cavity, we note that the additional production term related to shear-thinning becomes determinant for the instability only when  $n < 0.6$ . In this case the averaged Reynolds number is increasing and the core of the instability has moved to the lower half of the cavity. Interestingly, at neutral conditions the dissipation magnitude first increases for decreasing  $n$ , indicating increasing vorticity of the instability mode, while it decreases for the long-wavenumber mode found for  $n = 0.4$ . Looking at the budget at fixed  $Re$  and  $\kappa$ , Fig. 21b, we see how the pocket of instability is mainly created by increasing the production induced by the work of the Reynolds stresses against the base-flow shear.

## 5. Conclusions

Linear stability analysis of the lid-driven cavity containing non-Newtonian fluid has been performed for two different aspect ratios, namely  $\Gamma = 1$  (square cavity) and  $\Gamma = 0.25$  (shallow cavity). The former characterized by steady unstable modes at critical conditions, the latter by oscillating instabilities. The Carreau model has been chosen to model shear-thinning and shear-thickening fluids and the rheological parameters examined in the range  $0.4 \leq n \leq 1.4$  and  $\lambda = 1, 10$  and  $100$ . To investigate the instability mechanisms we consider both the classic equation for the evolu-

tion of the perturbation kinetic energy and the structural sensitivity of the instability, as introduced in [23].

In general, shear-thickening effects stabilize the flow, i.e. increase the critical  $Re$  both for the square and shallow cavity. Conversely, shear-thinning creates instabilities at lower Reynolds numbers. However, we see that at the lowest values of  $n$  considered the critical Reynolds number increases again. In particular, we observe for the square cavity that there exists an intermediate range of values of the power index  $n$  at which the instability mechanism is unaffected by non-Newtonian effects. This is demonstrated by examining the wave-maker of the instability as well as the spatial distribution of the kinetic energy production and dissipation. In addition, we show that the critical average Reynolds number, based on the average value of the local viscosity inside the cavity, is almost constant in this regime and, interestingly, becomes almost independent of the time constant  $\lambda$  (a result that actually applies to all values of  $n$  considered).

The increase of the critical Reynolds number for large shear-thinning can be explained by considering the non-Newtonian effects on the base flow: formation of thinner boundary layers close to the walls and reduction of the intensity of base-flow shear inside the cavity. In these cases, the extra-production of kinetic energy due to shear-thinning becomes determinant for the instability occurrence. For square cavities, we report a change from unsteady to oscillating critical modes already at moderate values of the power index  $n$  ( $n > 1.2$ ) associated to a significant increase of the spanwise scale of the unstable disturbance.

The neutral stability curve for the shallow cavity also show an increase of the critical Reynolds number at the lowest values of  $n$  considered, as mentioned above. In this case however, we find a new instability mode characterized by lower frequency and longer spanwise scale to be the first to become unstable when  $n < 0.5$ . The core of the instability has shifted from regions close to the upper driving wall to areas close to the lower wall. The same physical mechanisms as for Newtonian fluids appears to drive the instability for both shear-thinning and shear-thickening fluids otherwise for moderate non-Newtonian effects. Finally, we note that unlike in open flows, as for the flow past a circular cylinder [26], the analysis of the energy budget and the structural sensitivity, based on the superposition of the unstable mode and its adjoint, indicate the same critical region for the instability mechanism.

The linear analysis conducted here reveals the first flow bifurcation to a steady or oscillating three-dimensional flow. The present work is therefore being continued by considering the appearance of secondary instabilities and the effect of the shear-dependent viscosity on the unsteady regime at Reynolds number above the critical threshold. In addition, the flow sensitivity can be used to design passive control strategies to manipulate the flow inside the cavity.

## References

- [1] S. Albensoeder, H. Kuhlmann, H. Rath, Three-dimensional centrifugal-flow instabilities in the lid-driven-cavity problem, *Phys. Fluids* 13 (2001) 121–135.
- [2] O. Burggraf, Analytical and numerical studies of the structure of steady separated flows, *J. Fluid Mech.* 24 (1966) 113–151.
- [3] F. Pan, A. Acrivos, Steady flows in rectangular cavities, *J. Fluid Mech.* 28 (1967) 643–655.
- [4] U. Ghia, K. Ghia, C. Shin, High- $Re$  solutions for incompressible flow using the Navier–Stokes equation and a multigrid method, *J. Comput. Phys.* 48 (1982) 387–411.
- [5] R. Schreiber, H. Keller, Driven cavity flows by efficient numerical techniques, *J. Comput. Phys.* 49 (1983) 310–333.
- [6] J. Koseff, R. Street, Visualization studies of a shear driven three-dimensional recirculating flow, *J. Fluids Eng.* 106 (1984) 21–28.
- [7] J. Kim, P. Moin, Application of a fractional-step method to incompressible Navier–Stokes equations, *J. Comput. Phys.* 59 (1985) 308–323.
- [8] T. Chiang, W. Sheu, R. Hwang, Effect of Reynolds number on the eddy structure in a lid-driven cavity, *Int. J. Numer. Methods Fluids* 26 (1988) 557–579.
- [9] P. Shankar, M. Deshpande, Fluid mechanics in the driven cavity, *Ann. Rev. Fluid Mech.* 32 (2000) 93–136.
- [10] C. Aidun, N. Triantafillopoulos, J. Benson, Global stability of a lid-driven cavity with through-flow: flow visualization studies, *Phys. Fluids* 3 (1991) 2081–2091.
- [11] C. Aidun, J. Benson, Transition to unsteady nonperiodic state in a through-flow lid-driven cavity, *Phys. Fluids* 4 (1992) 2316–2319.
- [12] N. Ramanan, G. Homay, Linear stability of lid-driven cavity flow, *Phys. Fluids* 6 (1994) 2690–2701.
- [13] Y. Ding, M. Kawahara, Three-dimensional linear stability analysis of incompressible viscous flows using the finite element method, *Int. J. Numer. Methods Fluids* 31 (1999) 451–479.
- [14] H. Kuhlmann, M. Wanschura, H. Rath, Flow in two-sided lid-driven cavities: non-uniqueness, instabilities, and cellular structures, *Int. J. Numer. Methods Fluids* 336 (1997) 267–299.
- [15] H. Kuhlmann, S. Albensoeder, Strained vortices in driven cavities, *ZAMM, Z. Angew. Math. Mech.* 85 (2005) 387–399.
- [16] P. Pakdel, S. Spiegelberg, G. McKinley, Cavity flows of elastic liquids: two-dimensional flows, *Phys. Fluids* 9 (1997) 3123–3140.
- [17] P. Pakdel, G. McKinley, Cavity flows of elastic liquids: purely elastic instabilities, *Phys. Fluids* 10 (1998) 1058–1070.
- [18] A. Grillet, B. Yang, B. Khomami, E. Shaqfeh, Modeling of viscoelastic lid driven cavity flow using finite element simulations, *J. Non-Newtonian Fluid Mech.* 88 (1999) 99–131.
- [19] T.-W. Pan, J. Hao, Numerical simulation of a lid-driven cavity viscoelastic flow at high Weissenberg numbers, *CR Acad. Sci. Paris, Ser.* 344 (2007) 283–286.
- [20] K. Yapani, Y. Karasozen, B. Uludag, Finite volume simulation of viscoelastic laminar flow in a lid-driven cavity, *J. Non-Newtonian Fluid Mech.* 164 (2009) 51–65.
- [21] D. Santos, S. Frey, M. Naccache, P. Mendes, Numerical approximations for flow of viscoplastic fluids in a lid-driven cavity, *J. Non-Newtonian Fluid Mech.* 166 (2011) 667–679.
- [22] H. Mercan, K. Atalik, Flow structure for power-law fluids in lid-driven arch-shape cavities, *Korea–Australia Rheol. J.* 23 (2011) 71–80.
- [23] F. Giannetti, P. Luchini, Structural sensitivity of the first instability of the cylinder wake, *J. Fluid Mech.* 581 (2007) 167–197.
- [24] O. Marquet, D. Sipp, L. Jacquin, Sensitivity analysis and passive control of cylinder flow, *J. Fluid Mech.* 615 (2008) 221–252.
- [25] O. Marquet, M. Lombardi, J.-M. Chomaz, D. Sipp, L. Jacquin, Direct and adjoint global modes of a recirculation bubble: lift-up and convective non-normalities, *J. Fluid Mech.* 622 (2009) 1–21.
- [26] J. Pralits, L. Brandt, F. Giannetti, Instability and sensitivity of the flow around a rotating circular cylinder, *J. Fluid Mech.* 650 (2010) 513–536.
- [27] L. Brandt, J. Pralits, D. Sipp, O. Marguet, Effect of base flow variation on non-modal instability, *J. Fluid Mech.* 687 (2011) 503–528.
- [28] D. Sipp, O. Marquet, P. Meliga, A. Barbagallo, Dynamics and control of global instabilities in open flows: a linearized approach, *Appl. Mech. Rev.* 63 (2010) 030801.
- [29] H. Barnes, *Handbook of Elementary Rheology*, first ed., The University of Wales Institute of Non-Newtonian Fluid Mechanics, Aberystwyth, Wales, 2000.
- [30] F. Morrison, *Understanding Rheology*, 1st ed., Oxford University Press, Inc., Madison Avenue, New York, 2001.
- [31] D. Hill, Adjoint systems and their role in the receptivity, *J. Fluid Mech.* 292 (1995) 183–204.
- [32] M. Giles, N. Pierce, An introduction to the adjoint approach to design, *Flow, Turbulence and Combustion* 65 (2000) 393–415.
- [33] P. Fischer, J. Kruse, J. Mullen, H. Tufo, J. Lottes, S. Kerkemeier, Nek5000 – Open Source Spectral Element CFD Solver, 2008. <<https://nek5000.mcs.anl.gov/index.php/MainPage>>.